The Astrophysical Journal, 944:154 (15pp), 2023 February 20 https://doi.org/10.3847/1538-4357/acb43f

The Green Bank North Celestial Cap Survey. VII. 12 New Pulsar Timing Solutions

J. K. Swiggum[1,2], Z. Pleunis[3], E. Parent[4], D. L. Kaplan[1], M. A. McLaughlin[5,6], I. H. Stairs[7], R. Spiewak[8], G. Y. Agazie[1], P. Chawla[4], M. E. DeCesar[9], T. Dolch[10,11], W. Fiore[5,6], E. Fonseca[5,6], A. G. Istrate[12], V. M. Kaspi[4], V. I. Kondratiev[13], J. van Leeuwen[13], L. Levin[8], E. F. Lewis[5,6], R. S. Lynch[14], A. E. McEwen[1], H. Al Noori[15], S. M. Ransom[16], X. Siemens[17], and M. Surnis[18]

[1] Center for Gravitation, Cosmology, and Astrophysics, Department of Physics, University of Wisconsin-Milwaukee, P.O. Box 413, Milwaukee, WI 53201, USA; swiggumj@lafayette.edu
[2] Department of Physics, 730 High St., Lafayette College, Easton, PA 18042, USA
[3] Dunlap Institute for Astronomy & Astrophysics, University of Toronto, 50 St. George Street, Toronto, ON, M5S 3H4, Canada
[4] Department of Physics and McGill Space Institute, McGill University, Montreal, QC, H3A 2T8, Canada
[5] Dept. of Physics and Astronomy, West Virginia University, Morgantown, WV 26506, USA
[6] Center for Gravitational Waves and Cosmology, West Virginia University, Chestnut Ridge Research Building, Morgantown, WV 26506, USA
[7] Department of Physics and Astronomy, University of British Columbia, 6224 Agricultural Road, Vancouver, BC, V6T 1Z1 Canada
[8] Jodrell Bank Centre for Astrophysics, School of Physics and Astronomy, The University of Manchester, Manchester, M13 9PL, UK
[9] George Mason University, Fairfax, VA 22030, resident at the U.S. Naval Research Laboratory, Washington, D.C. 20375, USA
[10] Department of Physics, Hillsdale College, 33 E. College Street, Hillsdale, MI 49242, USA
[11] Eureka Scientific, 2452 Delmer Street, Suite 100, Oakland, CA 94602-3017, USA
[12] Department of Astrophysics/IMAPP, Radboud University, P.O. Box 9010, 6500 GL Nijmegen, The Netherlands
[13] ASTRON, the Netherlands Institute for Radio Astronomy, Oude Hoogeveensedijk 4, 7991 PD Dwingeloo, The Netherlands
[14] Green Bank Observatory, P.O. Box 2, Green Bank, WV 24494, USA
[15] Department of Physics, University of California, Santa Barbara, Santa Barbara, CA 93106, USA
[16] National Radio Astronomy Observatory, 520 Edgemont Rd., Charlottesville, VA 22903, USA
[17] Department of Physics, Oregon State University, Corvallis, OR 97331, USA
[18] Department of Physics, IISER Bhopal, Bhauri Bypass Road, Bhopal 462066, India
Received 2022 December 7; accepted 2023 January 15; published 2023 February 21

Abstract

We present timing solutions for 12 pulsars discovered in the Green Bank North Celestial Cap 350 MHz pulsar survey, including six millisecond pulsars (MSPs), a double neutron star (DNS) system, and a pulsar orbiting a massive white dwarf companion. Timing solutions presented here include 350 and 820 MHz Green Bank Telescope data from initial confirmation and follow-up, as well as a dedicated timing campaign spanning 1 yr PSR J1122−3546 is an isolated MSP, PSRs J1221−0633 and J1317−0157 are MSPs in black widow systems and regularly exhibit eclipses, and PSRs J2022+2534 and J2039−3616 are MSPs that can be timed with high precision and have been included in pulsar timing array experiments seeking to detect low-frequency gravitational waves. PSRs J1221−0633 and J2039−3616 have Fermi Large Area Telescope gamma-ray counterparts and also exhibit significant gamma-ray pulsations. We measure proper motions for three of the MSPs in this sample and estimate their space velocities, which are typical compared to those of other MSPs. We have detected the advance of periastron for PSR J1018−1523 and therefore measure the total mass of the DNS system, $m_{\rm tot} = 2.3 \pm 0.3\ M_{\odot}$. Long-term pulsar timing with data spanning more than 1 yr is critical for classifying recycled pulsars, carrying out detailed astrometry studies, and shedding light on the wealth of information in these systems post-discovery.

Unified Astronomy Thesaurus concepts: Binary pulsars (153); Millisecond pulsars (1062); Gamma-ray sources (633); Pulsar timing method (1305)

1. Introduction

The Green Bank North Celestial Cap (GBNCC) pulsar survey began in 2009 and is largely complete, having discovered 194 pulsars so far. Using the 100 m Green Bank Telescope (GBT), the survey has covered the full sky accessible to the Green Bank Observatory, all declinations $\delta > -40°$. Operating at a relatively low center frequency of 350 MHz, individual beams are 36′ across and the large survey region (85% of the celestial sphere) can be covered efficiently with ≈125,000 overlapping pointings. With overhead, this comes out to ≈5500 hr of scheduled telescope time. Only a few observations remain, reobserving pointings being significantly affected by radio frequency interference (RFI).

For each 120 s sky pointing, data are collected in search mode with 4096 frequency channels spanning 100 MHz of bandwidth centered at 350 MHz. Total intensities are sampled every 81.92 μs. Data are transferred to McGill University and processed using large allocations on Compute Canada supercomputers. Searches for both periodic and transient signals are carried out at a range of trial dispersion measures (DMs) with a pipeline based on the PRESTO[19] software package (Ransom et al. 2002).

A full description of the survey and initial sensitivity projections can be found in Stovall et al. (2014). Timing solutions for GBNCC discoveries are included there, in Kaplan et al. (2012), Karako-Argaman et al. (2015), and, more recently, Kawash et al. (2018), Lynch et al. (2018), Aloisi et al. (2019), and Agazie et al. (2021). The first fast radio burst discovery (FRB20200125A) is described in Parent et al.

[19] https://www.cv.nrao.edu/~sransom/presto/

(2020), and McEwen et al. (2020) provides a census of GBNCC discoveries at the time of publication and detailed survey sensitivity analysis. Published standard profiles, pulse times of arrival (TOAs), and timing models from most of these previous studies are publicly available on GitHub,[20] linked from the GBNCC discoveries page.[21]

The primary science goal of the GBNCC pulsar survey is discovering millisecond pulsars (MSPs), a class of old neutron stars (NSs) spun up through mass transfer from a donor companion (Alpar et al. 1982). High-precision MSP discoveries are critical for the detection of a stochastic nanohertz gravitational wave (GW) background. Such a background signal would likely come from coalescing supermassive black holes (Jaffe & Backer 2003), relic cosmological GWs (e.g., Grishchuk 2005), and/or cosmic strings (Maggiore 2000). Nanohertz GW detection efforts with pulsar timing arrays (PTAs) span the globe; the US–Canada effort, the North American Nanohertz Observatory for Gravitational waves (NANOGrav), most recently published a 12.5 yr data release (Alam et al. 2021a, 2021b) where the first hints of a GW background may be present (Arzoumanian et al. 2020). The latest combined International Pulsar Timing Array (IPTA) data release (DR2; Perera et al. 2019), comprised of PTA data sets from groups in Europe, Australia, and North America, shows similar hints of the GW background (Antoniadis et al. 2022). The most effective way to increase PTA sensitivity to the nanohertz GW background is by adding MSPs to the array (Siemens et al. 2013). NANOGrav aims to add four MSPs to its array each year, and thus relies heavily on pulsar surveys like GBNCC to provide these new sources.

The GBNCC pulsar survey also aims to find exotic new binary systems that push the boundaries of our understanding in various areas. Double neutron star (DNS) systems can place constraints on NS kick distributions (Tauris et al. 2017; Vigna-Gomez et al. 2018), provide laboratories for testing theories of gravity (see Will 2014 for a review), and inform NS merger rates (Burgay et al. 2003; Kalogera et al. 2004; Chruslinska et al. 2018; Mandel & Broekgaarden 2022). Eclipsing binaries offer opportunities to probe material surrounding the companion in/around the eclipse. In some cases, pulsar binaries can also constrain the equation of state of supranuclear matter via NS mass measurements (Cromartie et al. 2020). All of these systems bring into focus the wide variety of evolutionary scenarios and offer possible explanations for open questions (e.g., the origin of isolated MSPs), and, in many cases, even richer information can be gleaned from multifrequency follow-up (Swiggum et al. 2017). In this study, we have specifically targeted new discoveries with spin periods $<$200 ms for timing follow-up to identify recycled pulsars, distinguish between isolated and binary systems, and start tackling some of these broader science goals.

Section 2 describes the confirmation and timing follow-up for 12 discoveries, including flux density and spectral index measurements based on observations at 350 and 820 MHz. Timing model parameters and their values are presented in Section 3, including further analysis for three MSP systems where proper motions were detected. Section 4 describes the process we used to search for gamma-ray counterparts (and pulsations, where appropriate), as well as individual source classifications and interesting features based on timing models. We conclude in Section 5 and outline some future work that is underway.

[20] https://github.com/GBNCC/data
[21] http://astro.phys.wvu.edu/GBNCC

2. Pulsar Timing Observations and Analysis

2.1. Observations

The 12 discoveries described in this paper were initially flagged as periodicity candidates, then confirmed with GBT scans at 350 MHz. All were used regularly as test sources during survey observations and folded in real time to monitor the RFI environment and survey data quality. These data served a dual purpose since they were also included in our timing analysis (Section 2.4). Test scans conducted at 350 MHz used 81.92 μs time resolution and 4096 channels across 100 MHz of bandwidth.

Following confirmation scans at 350 MHz, pulsar positions were improved using an on-the-fly mapping technique described in Swiggum & Gentile (2018), resulting in position uncertainties of $\approx 1'$–$3'$. Improved localization ensures that the pulsar is closer to the telescope's boresight in observations that follow; it provides additional flexibility in choice of observing frequency (since telescope beam size is inversely proportional to the chosen center frequency), ensures higher signal-to-noise ratio (S/N) detections and thus more efficient follow-up, and facilitates the process of finding an initial timing solution.

Afterwards, timing data were collected using the GBT (project code 17B−285; PI: J. Swiggum) at 820 MHz with 2048 channels across 200 MHz bandwidth and 40.96 μs time resolution. For PSR J0742+4110, timing data were included from a previous GBT timing campaign using the same setup (project code 15A−376; PI: L. Levin). Each pulsar was observed with a monthly cadence over a full year; high-cadence sessions were also included to observe each pulsar 4–5 times over one week to establish initial phase connection and aid in solving binary parameters, where necessary.

2.2. Measured Flux Densities: S_{350} and S_{820}

Since data collection for this study was sometimes opportunistic and/or coherent timing solutions for the sources included were not initially available (see Section 2.1), observations were predominantly conducted in search mode and time was not spent on polarization/flux-density calibration. Therefore, we estimate 350 and 820 MHz flux densities (S_{350} and S_{820}) for each source using summed, total-intensity pulse profiles (see Figure 1) and the radiometer equation as follows.

As in Lorimer & Kramer (2004), flux densities at respective observing frequencies, S_ν, are computed here using the radiometer equation:

$$S_\nu = \beta \frac{(\mathrm{S/N})\, T_{\mathrm{sys}}}{G(\theta)\sqrt{n_{\mathrm{p}}\, t_{\mathrm{int}}\, \Delta f}} \sqrt{\frac{\delta}{1-\delta}}, \quad (1)$$

where the S/N is measured from summed pulse profiles, shown in Figure 1, using the same technique as described in McEwen et al. (2020). System temperature (T_{sys}) is the sum of sky temperature (T_{sky}) and receiver temperature (T_{rec}). We use `PyGDSM`[22] to get T_{sky}, including the contribution from the cosmic microwave background, at each source position and observing frequency based on Zheng et al. (2017). At 350/

[22] https://github.com/telegraphic/pygdsm

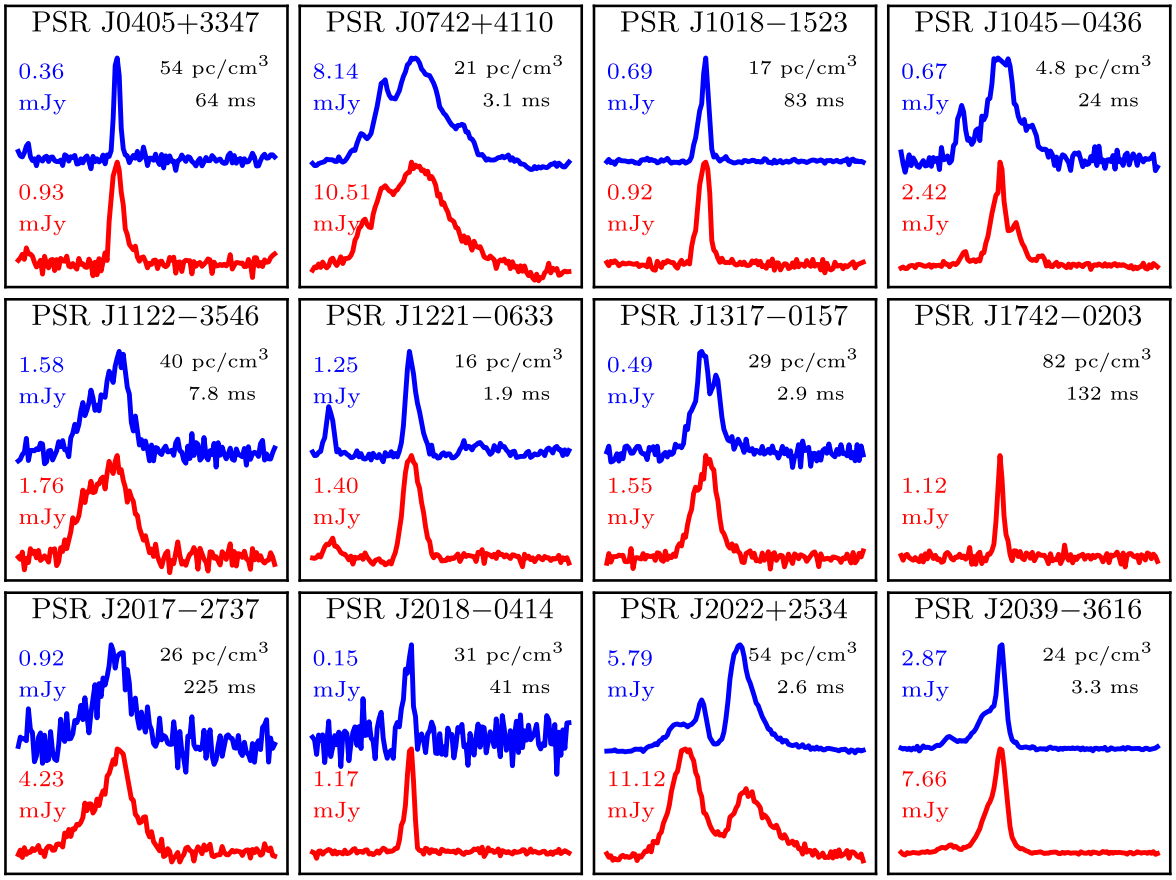

Figure 1. Summed pulse profiles depicting intensity over a full rotation. Profiles have been scaled by their respective maximum intensities to make it easier to compare their shapes. They were generated using all 350 MHz (red; bottom of each panel) and 820 MHz (blue; top) data available, with corresponding flux densities in the same colors listed to the left in millijanskys. To the right of each profile, the pulsar's DM is given in parsecs per cubic centimeter and spin period in milliseconds. PSR J1742−0203 was never detected at 820 MHz.

820 MHz, $T_{\rm rec} = 23/22$ K, respectively (see Figure 3 in the GBO Proposer's Guide).[23] Duty cycle (δ) here is the fraction of the integrated profile where the pulsar's signal is present, $\delta = n_{\rm on}/n_{\rm bin}$. Degradation due to digitization is reflected by $\beta = 1.3$, the number of summed polarizations is $n_{\rm p} = 2$, the effective bandwidth is $\Delta f = 70/175$ MHz at 350/820 MHz, respectively (accounting for common RFI zapping), and the GBT's gain along the boresight, $G(0) = 2$ K Jy^{-1}. Since timing positions were not measured until relatively late in our follow-up programs, observing catalog positions—even after improvements—could be offset by several arcminutes. These offsets translate to some amount of degradation in the effective gain. Gaussian functions with FWHM equal to those of the 350/820 MHz beams (FWHM = $36'/15'$, respectively) provide good approximations of degradation as a function of position offset. For our flux-density analysis, we generate integrated pulse profiles using observations within $\theta = 7'/3'$ at 350/820 MHz, respectively, which translates to a 10% degradation in gain. In several cases, tolerating larger offsets was required to integrate a sufficient number of observations, and larger degradation factors were applied when calculating S_{820} for PSRs J0742+4110, J1122−3546, and J2017−2737.

Table 1 lists total integration times ($t_{\rm int}$) for individual sources for each observing frequency, as well as measured duty cycles (δ) and resulting flux densities and spectral indices (α, where $S_\nu \propto \nu^\alpha$). To estimate uncertainties, we use standard error propagation, assuming $\sigma_{\Delta f} = 10$ MHz (due to transient sources of RFI, effective bandwidth can vary), $\sigma_{T_{\rm sys}} = 5$ K, and $\sigma_G = 0.1$–0.5 K Jy^{-1}, depending on typical observing position offsets.

To check our measurements for consistency, we looked at the literature and other catalogs for matching detections and flux-density measurements. In a census of MSP flux densities with MeerKAT, Spiewak et al. (2022) found $S_{1400} = 0.50 \pm 0.04$ mJy for PSR J2039−3616, and a spectral index of -2.0 ± 0.4. These values, scaled to 350 MHz, are completely consistent with the S_{350} reported here, but our S_{820} measurement (and therefore spectral index) is only consistent at the 2–3σ level. PSR J2022+2534 was detected in the Rapid ASKAP Continuum Survey, RACS-low (888 MHz; Hale et al. 2021) with $S_{888} = 3.6 \pm 0.3$ mJy, which is consistent with our measurement at the $\approx 2\sigma$ level. Other catalogs such as the TIFR GMRT Sky Survey and LOFAR Two-meter Sky Survey did not have any unidentified radio sources corresponding to those in this sample. Finally, we compared the S_{350} measurements here with those presented in McEwen et al. (2020) and find broad consistency at the $\approx$1–2σ level (except for PSRs J0742+4110 and J2039−3616, whose values here are about 5 times higher). At 350 MHz both of these pulsars have estimated scintillation timescales ($\approx$250 and $\approx$120 s, respectively) near the length of a GBNCC survey observation time (120 s), so it is

[23] https://www.gb.nrao.edu/scienceDocs/GBTpg.pdf

Table 1
350 and 820 MHz Flux Densities, Spectral Index Measurements

PSR	350 MHz			820 MHz			
	t_{int} (s)	δ	S_{350} (mJy)	t_{int} (s)	δ	S_{820} (mJy)	α
J0405+3347	3309.8	0.17	0.93(13)	584.0	0.08	0.36(7)	−1.1(3)
J0742+4110	5906.3	0.81	10.5(1.5)	5480.4	0.86	8.1(1.8)	−0.3(3)
J1018−1523	2583.0	0.12	0.92(14)	3686.3	0.16	0.69(14)	−0.3(3)
J1045−0436	14112.3	0.45	2.4(4)	4944.2	0.41	0.67(13)	−1.5(3)
J1122−3546	4015.8	0.38	1.8(3)	1188.0	0.31	1.6(8)	−0.1(7)
J1221−0633	10225.4	0.32	1.4(2)	5841.1	0.59	1.2(2)	−0.1(3)
J1317−0157	9557.0	0.30	1.6(2)	4309.6	0.28	0.49(9)	−1.4(3)
J1742−0203	4539.9	0.11	1.12(15)	⋯	(0.06)	<0.2	< -1.5
J2017−2737	3935.3	0.47	4.2(6)	564.0	0.38	0.92(2)	−1.8(3)
J2018−0414	8350.4	0.12	1.17(16)	564.0	0.09	0.15(3)	−2.4(3)
J2022+2534	6534.4	0.66	11.1(1.4)	3888.0	0.66	6(1)	−0.8(3)
J2039−3616	7637.0	0.45	7.7(1.1)	4068.6	0.48	2.9(5)	−1.2(3)

Notes. Total integration time (t_{int}) used to generate profiles, and measured duty cycles (δ), flux densities (S_{350}/S_{820}), and spectral indices (α) are listed for pulsars at each observing frequency included in our analysis. Since J1742−0203 was not detected at 820 MHz, we place limits on S_{820} and α for this pulsar, assuming a typical duty cycle, $\delta = 0.06$.

plausible they were scintillated down during their discovery scans.

Due to systematic uncertainties often present in estimating flux densities using the radiometer equation, measured values can be discrepant by factors of 2 or more. Taking this into account, our measurements are in reasonable agreement with those from other radio surveys and previous studies.

Finally, we note some surprise at the fact that none of the 350 MHz summed profiles in Figure 1 exhibit significant scatter broadening compared to their 820 MHz counterparts. Electron density models (NE2001/YMW16) predict scattering timescales at the level of 5%–30% of a rotation in most cases, but >50% for J2022+2534. Many of these sources are well off the Galactic plane (see Table 3), where electron density models tend to have higher uncertainties, but this may also be a selection effect. Sources that exhibit less scattering are more likely to be detected in the 350 MHz GBNCC pulsar survey.

2.3. Detections and Preliminary Binary Parameters

Before timing solutions were available, periodicity searches were carried out using dedispersed time series from each epoch, since many sources were known to be in binary systems and therefore their apparent spin periods would change between sessions. First, RFI was masked automatically using `rfifind` and the known DM was applied to produce topocentric and barycentric time series with `prepdata`. Periodicity candidates were generated with `accelsearch`. After finding a candidate period close to the discovery value, the raw data were folded using `prepfold` and the candidate periodicity refined by allowing a fine search in period and period derivative.

Binary systems were identified by their time-variable barycentric spin periods, which were compiled and analyzed for each source using the "roughness" method described in Bhattacharyya & Nityananda (2008). Roughness,

$$\mathcal{R} = \sum_{i=1}^{n-1} [P_{obs}(i) - P_{obs}(i+1)]^2, \quad (2)$$

where P_{obs} represents a set of observed spin periods, sorted by their orbital phase using corresponding observation epochs and trial orbital period values. Roughness was calculated for many trial orbital periods and minimized to provide a reasonable guess for the best initial value. A full set of preliminary binary parameters followed for each binary system by devising a rough model that matched the shape of measured spin period versus orbital phase (ϕ_{orb}; see Figure 2).

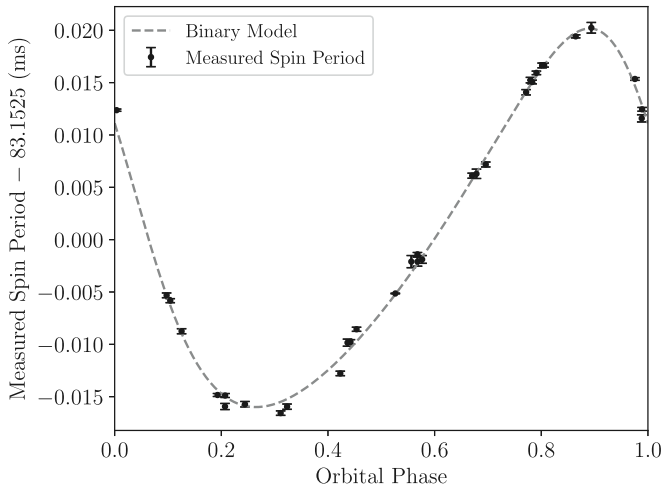

Figure 2. Spin period measurements and 1σ uncertainties for PSR J1018−1523 plotted as a function of orbital phase. The gray dashed line represents the expected apparent spin period changes as a function of orbital phase (mean anomaly), given a preliminary set of orbital parameters similar to those reported in Table 6.

2.4. Timing Analysis

Before timing ephemerides were available for discoveries, individual scans were processed as described in Section 2.3, and three TOAs were generated per 5–10 minute observation with `get_TOAs.py` from `PRESTO`. In order to accurately determine arrival times, a standard profile is cross-correlated with the observed signal in the Fourier domain (Taylor 1992). In this initial stage, a standard profile was generated for each pulsar with `pygaussfit.py`, fitting Gaussian components to the highest S/N profile available. Due to frequency-dependent profile evolution, different standard profiles were used for calculating TOAs at 350 and 820 MHz as necessary. Three

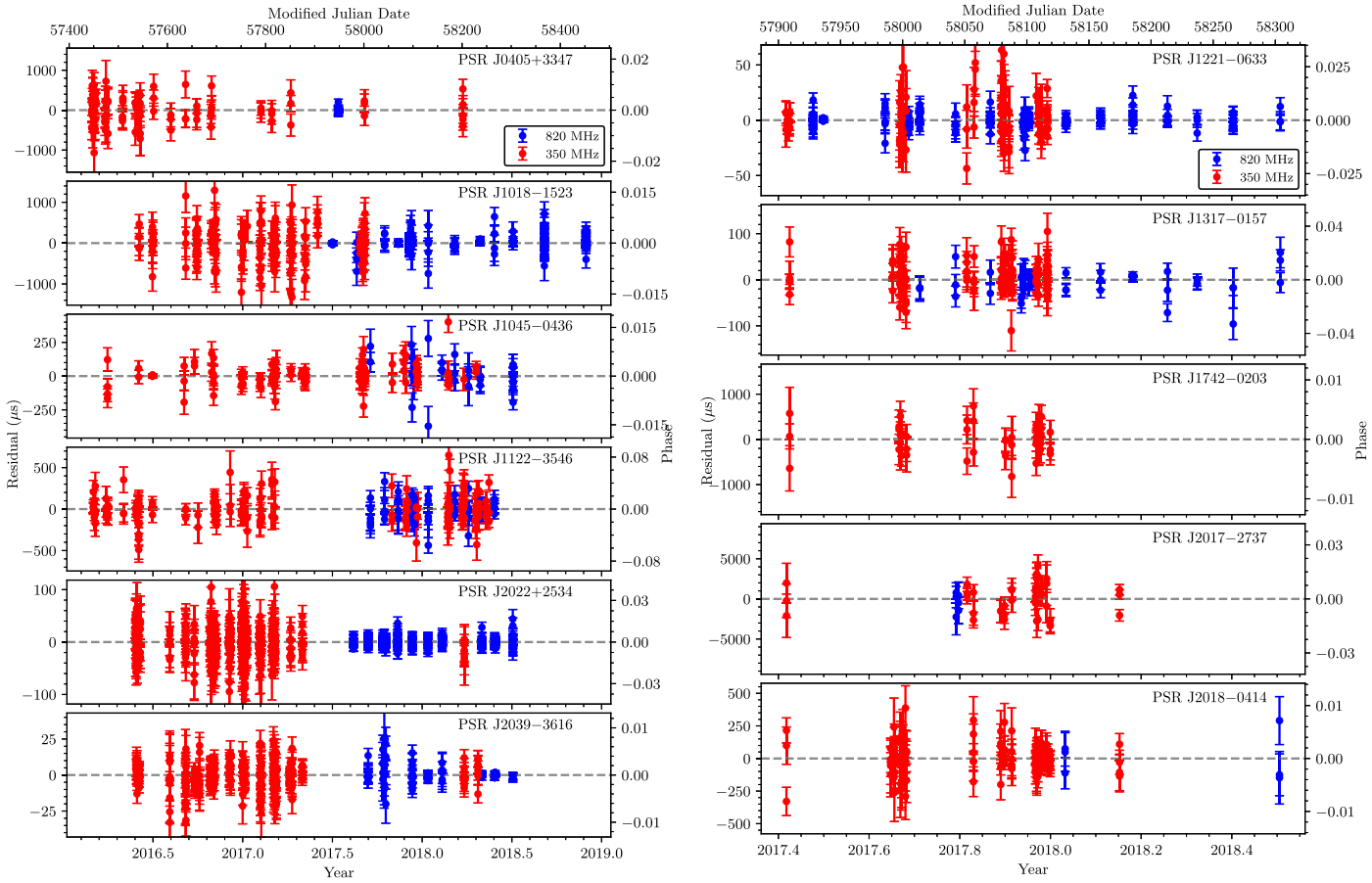

Figure 3. (a) Timing residuals for PSRs J0405+3347, J1018−1523, J1045−0436, J1122−3546, J2022+2534, and J2039−3616, from observations at 350 MHz (red) and 820 MHz (blue), respectively. Error bars represent 1σ uncertainties on individual TOA measurements. Note: timing residuals for PSR J0742+4110 are not plotted here since those data come from an earlier study (GBT project code 15A−376; PI: L. Levin) and span a very different period of time. (b) Timing residuals for PSRs J1221−0633, J1317−0157, J1742−0203, J2017−2737, and J2018−0414, from observations at 350 MHz (red) and 820 MHz (blue), respectively. Error bars represent 1σ uncertainties on individual TOA measurements.

TOAs per epoch allowed fits for spin frequency on a per-epoch basis, facilitating phase connection over short timescales—initially days to weeks. These coherent timing solutions were then extended across the full data span using the `TEMPO`[24] pulsar timing software.

With coherent timing solutions in hand, individual scans were refolded and manipulated as follows using processing routines available in the `PSRCHIVE`[25] software suite (Hotan et al. 2004). First, RFI was carefully excised using `pazi`, then scans were scrunched down to 3–5 subintegrations and 2–4 subbands, S/N permitting, ensuring that the pulsar signal was detectable in each of these divisions. For each pulsar, detections were summed coherently at respective observing frequencies using `psradd`, which uses ephemerides to phase-align observations from different epochs, to create averaged profiles (see Figure 1 and Section 2.2 for details regarding profile analysis). Noise-free standard profiles at 350 and 820 MHz were generated by fitting Gaussian components to averaged profiles, and the two templates were aligned using `pas`. Standard profiles were cross-correlated with folded, cleaned, and scrunched data to produce a final set of TOAs with `pat`. Since standard profiles for the respective observing bands were aligned as part of this process, we did not fit for any time offsets ("jumps") between corresponding TOAs; however, observing-mode-dependent instrumental offsets were taken into account (e.g., an 61.44 μs instrumental delay between 350/820 MHz data collected in incoherent mode). Parameter fitting and refinement was conducted using `TEMPO`, with the DE430 solar system ephemeris and TT(BIPM) time standard implemented therein.

3. Results

3.1. Timing Model Fitting

The final sets of timing residuals (differences between measured/expected TOA) from this refinement process are plotted in Figure 3. Results from fitting for spin and astrometric parameters are listed in Tables 2 and 3, respectively, and the corresponding derived parameters can be found in Table 4. In some cases, the reduced χ^2 values were relatively far from 1, so TOA uncertainties have been scaled by multiplicative error factors (EFACs; see Table 2) to force $\chi^2_{\rm red} = 1$. This scaling also impacts uncertainties on parameters measured via pulsar timing.

For three MSPs (PSRs J0742+4110, J2022+2534, and J2039−3616), timing precision was sufficient to measure their proper motions in ecliptic longitude and latitude, μ_λ and μ_β. Proper motion is detectable with pulsar timing and manifests itself as a growing sinusoid in the pulsar timing residuals.

[24] http://tempo.sourceforge.net/
[25] http://psrchive.sourceforge.net/

Table 2
Rotational and Timing Parameters of GBNCC Pulsars

PSR	ν (Hz)	$\dot{\nu}$ (Hz s^{-1})	Epoch (MJD)	Data Span (MJD)	rms Residual (μs)	$N_{\rm TOA}$	EFAC
J0405+3347	15.6362508979(4)	$-4.0(3) \times 10^{-17}$	57824	57445–58201	174.6	108	1.0597
J0742+4110	318.55889711523(3)	$-6.791(4) \times 10^{-16}$	57169	56044–58294	12.1	222	1.3308
J1018−1523	12.02609153542(3)	$-1.58(8) \times 10^{-17}$	57998	57542–58452	65.8	425	1.1679
J1045−0436	41.58433482255(5)	$-1.36(1) \times 10^{-16}$	57891	57478–58304	45.5	153	1.3027
J1122−3546	127.5824382850(3)	$-2.48(9) \times 10^{-16}$	57858	57449–58266	120.4	250	1.2736
J1221−0633	516.918832068(1)	$-1.42(2) \times 10^{-15}$	58105	57906–58304	4.4	264	1.2066
J1317−0157	343.850032475(2)	$-6.5(4) \times 10^{-16}$	58107	57909–58304	23.5	164	1.2961
J1742−0203	7.59822533(3)	$-8.6(7) \times 10^{-15}$	58014	57909–58118	285.6	45	1.0817
J2017−2737	4.4538744(1)	$-1.21(1) \times 10^{-13}$	58041	57906–58174	1802.8	47	1.6155
J2018−0414	24.623136942(1)	$-4(2) \times 10^{-17}$	58105	57906–58303	73.0	136	1.0262
J2022+2534	377.93812391457(8)	$-8.80(2) \times 10^{-16}$	57919	57535–58303	10.0	744	1.0354
J2039−3616	305.33963750348(3)	$-7.845(8) \times 10^{-16}$	57920	57537–58303	4.3	375	1.0349

Note. All timing models use the DE430 solar system ephemeris and are referenced to the TT(BIPM) time standard. Values in parentheses are the 1σ uncertainty in the last digit as reported by TEMPO. Multiplicative error factors (EFACs) listed here were applied to TOA uncertainties, forcing $\chi^2_{\rm red} = 1$.

Typically this signature is only detectable after timing pulsars over longer timespans ($\gtrsim$3 yr) or for young pulsars that have substantial kick velocities, but proper motion can also be detected over 1–2 yr timespans for nearby MSPs with high-precision TOAs, as is the case here.

Total proper motions and DM distances ($D_{\rm DM}$) for these MSPs were used to compute transverse velocities ($v_{\rm t}$; see Table 5). Transverse motion translates to an apparent spin-down due to a pulsar's motion relative to the solar system barycenter; this is called the Shklovskii effect (Shklovskii 1970), $\dot{P}_{\rm S}$, and is typically only significant for nearby MSPs whose $\dot{P}$ values already tend to be small. A pulsar's acceleration in the Galactic potential can also contribute to the measured spin-down. However, this factor, $\dot{P}_{\rm G}$, is usually only significant for relatively distant MSPs. We follow the same procedure as described in Guo et al. (2021) to calculate $\dot{P}_{\rm G}$, which includes an approximation for the vertical component of Galactic acceleration (Holmberg & Flynn 2004) and the latest values for the distance between the Sun and Galactic center and the circular velocity of the Sun ($R_0 = 8.275 \pm 0.034$ kpc and $\Phi_0 = 240.5 \pm 4.1$ km s^{-1}, respectively; Reid & Brunthaler 2020; GRAVITY Collaboration et al. 2021). In Table 5, we calculate μ_λ, μ_β, and v_t for PSRs J0742+4110, J2022+2534, and J2039−3616, then use NE2001 (Cordes & Lazio 2002) and YMW16 (Yao et al. 2017) distance models[26] to determine intrinsic spin-down values, $\dot{P}_{\rm int}$, by subtracting the $\dot{P}_{\rm S}$ and $\dot{P}_{\rm G}$ components from the measured $\dot{P}$. Finally, we compute the resulting surface magnetic field ($B_{\rm surf}$), characteristic age ($\tau_{\rm c}$), and spin-down luminosity ($\dot{E}$) using each pulsar's measured spin period, P, and $\dot{P}_{\rm int}$.

For most of the binary systems presented here, we used the ELL1 timing model (Lange et al. 2001), which parameterizes orbital parameters in terms of the epoch of the ascending node ($T_{\rm asc}$) and first and second Laplace–Lagrange parameters (ϵ_1 and ϵ_2). This is a convenient prescription for low-eccentricity systems with short-period orbits. For J1018−1523, which we suspect is a new DNS system, we employed the DD model (Damour & Deruelle 1986) and fit for one relativistic parameter (advance of periastron, $\dot{\omega}$), in addition to the usual five Keplerian parameters used to describe binary orbits. The results of the binary parameter fits can be found in Tables 6 and 7.

In several cases, TOAs from discovery scans were included to improve spin-down ($\dot{\nu}$) measurements (see, e.g., PSRs J1317−0157, J1742−0203, J2017−2737, and J2018−0414). A Taylor expansion was used to express each pulsar's expected phase as a function of time, given initial measurements for spin frequency and frequency derivative and their uncertainties from our timing campaign. In each case where discovery TOAs were included, we ensured that the pulse phase uncertainties accumulated over 3–6 month gaps amounted to $\ll$1 rotation. Additional analysis and interpretation of timing models and parameters measured for individual sources can be found in Section 4.

3.2. Fermi-LAT Counterparts

The last decade has seen the discovery of a profusion of gamma-ray pulsars[27] thanks to the Large Area Telescope (LAT; Atwood et al. 2009) on the Fermi Gamma-ray Space Telescope. LAT has been continuously imaging the sky in the energy range from ∼20 MeV to 1 TeV since 2008.

Several pulsars in that rich data set have been identified through deep radio searches targeting Fermi-LAT unidentified point sources (e.g., Ransom et al. 2011; Kerr et al. 2012; Ray et al. 2012; Camilo et al. 2015; Cromartie et al. 2016; Pleunis et al. 2017; Deneva et al. 2021). However, high levels of background contamination—particularly in the Galactic plane, where most pulsars reside—may cause gamma-ray pulsars to be confused and undetectable as point sources. An alternative approach that has proven fruitful is by selecting gamma-ray photons coming from the position of known radio pulsars and phase-folding the data using coherent timing solutions derived from the radio data (e.g., Abdo et al. 2010a, 2013; Smith et al. 2019). In this work, we have searched for high-energy counterparts to our pulsars through both identification methods.

We inspected the Fermi-LAT 12 yr gamma-ray source catalog (4FGL-DR3; Abdollahi et al. 2022) to identify objects spatially coincident with the timing positions of the pulsars we derived from the GBT data. Three of the 12 pulsars have positions coincident with Fermi point sources. The timing positions of PSRs J1221−0633 and J2039−3616 are within the 68% confidence region of the sources 4FGL J1221.4−0634

[26] See also https://pulsar.cgca-hub.org/compute.

[27] See http://tinyurl.com/fermipulsars for an overview.

Table 3
Coordinates and Dispersion Measures of GBNCC Pulsars

PSR	Measured			Derived			
	λ (°)	β (°)	DM (pc cm^{-3})	α (J2000)	δ (J2000)	ℓ(°)	b (°)
J0405+3347	65.908034(6)	12.70753(3)	53.596(3)	$04^{h}\,05^{m}\,29\overset{s}{.}57$	+33°47′00.″3	162.78	−13.68
J0742+4110	110.1469948(7)	19.502018(1)	20.8135(2)	$07^{h}\,42^{m}\,12\overset{s}{.}19$	+41°10′14.″9	178.13	26.57
J1018−1523	162.497241(2)	−24.093012(8)	17.158(2)	$10^{h}\,18^{m}\,12\overset{s}{.}72$	−15°23′10.″2	257.13	33.53
J1045−0436	164.7121434(8)	−11.510665(4)	4.8175(9)	$10^{h}\,45^{m}\,57\overset{s}{.}92$	−04°36′23.″4	254.46	46.12
J1122−3546	187.868380(2)	−36.102612(4)	39.5868(7)	$11^{h}\,22^{m}\,17\overset{s}{.}24$	−35°46′31.″2	283.30	23.67
J1221−0633	187.5164776(2)	−3.900195(2)	16.43241(6)	$12^{h}\,21^{m}\,24\overset{s}{.}76$	−06°33′51.″7	289.68	55.53
J1317−0157	198.6676339(8)	5.786217(9)	29.4008(2)	$13^{h}\,17^{m}\,40\overset{s}{.}45$	−01°57′30.″1	316.23	60.23
J1742−0203	265.2820(4)	21.3053(2)	81.82	$17^{h}\,42^{m}\,24\overset{s}{.}53$	−02°03′43.″2	22.99	14.33
J2017−2737	300.243(2)	−7.600(4)	25.82(5)	$20^{h}\,17^{m}\,01\overset{s}{.}63$	−27°30′49.″2	15.23	−29.91
J2018−0414	305.834964(6)	15.00891(1)	30.914(1)	$20^{h}\,18^{m}\,10\overset{s}{.}41$	−04°14′12.″7	39.23	−21.20
J2022+2534	316.3805463(2)	43.4494254(2)	53.6623(1)	$20^{h}\,22^{m}\,33\overset{s}{.}26$	+25°34′42.″5	66.10	−6.54
J2039−3616	302.72326687(7)	−17.2460168(3)	23.96332(7)	$20^{h}\,39^{m}\,16\overset{s}{.}58$	−36°16′17.″2	6.33	−36.52

Notes. Ecliptic coordinates use the IERS2010 value of the obliquity of the ecliptic referenced to J2000 (Capitaine et al. 2003). Values in parentheses are the 1σ uncertainty in the last digit as reported by `TEMPO`. In some cases, the reported precision goes beyond month–year timescale changes in DM that might be expected due to interstellar medium effects (see, e.g., Jones et al. 2017), but modeling those changes goes beyond the scope of this work.

(detection significance of 23.4 σ) and 4FGL J2039.4−3616 (15.2 σ), respectively. Both 4FGL sources have pulsar-like power-law spectra with subexponential cutoffs. The third potential association is PSR J1317−0157, colocated within the 95% confidence region of 4FGL J1317.5−0153 (9.4σ detection). This source has a log-normal spectrum, which is not as common as the subexponential cutoff power law among known gamma-ray pulsars. The likelihood of the 4FGL point sources being counterparts to the pulsars in terms of pulsar energetic and Fermi-LAT sensitivity is examined further below. However, we first describe the method we used to search for high-energy pulsed emission through the phase-folding of the Fermi-LAT photons.

For all pulsars we retrieved LAT photons[28] within 3° of the timing positions collected from 2008 August 5 (≈the start of the mission) to 2022 August 5. We selected photons with an energy E_γ in the range $0.1 < E_\gamma < 500$ GeV and applied the standard events screening recommended by the Fermi-LAT team.[29] Good time intervals (where the telescope observed nominally) were selected using `gtmktime` and photon arrival times were corrected to the Earth's geocenter with the `gtbary` tool.

Using PINT's `fermiphase`[30] tool, we assigned to each photon a probability of being emitted by the pulsar (i.e., weighted) following the method from Bruel (2019). Weight computations are based on the photon energy and angular separation from the target position for an assumed spectral distribution. The only free parameter in the weight model is the $\mu_E = \log_{10}(E_{\rm ref}/1{\rm MeV})$, where $E_{\rm ref}$ is the reference energy at which the distribution of photon weights peaks (see Equation (11) of Bruel 2019). The bulk of the known gamma-ray pulsars have $\mu_E \approx 3.6$ (equivalently, $E_{\rm ref} \approx 4$ GeV), but hard-spectrum sources in highly confused regions may favor $\mu_E > 4$.

Considering that the pulsars in this work are located at various Galactic latitudes and therefore are subject to different types of background contamination, we phase-folded the LAT data set with four trial μ_E in the weight calculation, with $\mu_E \in \{2.8, 3.2, 3.6, 4.0\}$. The weighted H-test statistic (de Jager & Busching 2010; Bruel 2019) was calculated to assess the significance of the pulsations. An additional filtering of low-weight photons was then applied in order to identify the minimum photon weight, $w_{\rm min}$, that maximizes the H-test (to value $H_{\rm max}$) for each trial μ_E. To avoid potential sensitivity losses due to long-term timing effects (e.g., proper motion) that are not modeled in the timing solutions, we repeated the same procedure but this time selecting only events within the validity range of the radio ephemerides.

Following the analysis of Smith et al. (2019), who used a similar approach to fold over a thousand pulsars and examine their H-test distribution to identify the ideal selection criteria to reject false positives, we dismissed candidates with $H_{\rm max} < 25$ (equivalent to a ≈4σ detection) across all trial combinations (w, μ_E). Further optimization was performed for statistically significant detections by performing a finer search in trial μ_E.

Among the 12 pulsars presented in this work, pulsations were detected in two pulsars, PSRs J1221−0633 and J2039−3616, which are two of the three pulsars that are colocated with 4FGL sources. These, along with the nondetection of pulsations in PSR J1317−0157 colocated with 4FGL J1317.5−0153, are discussed below. Apart from PSRs J1221−0633 and J2039−3616, no significant pulsations were detected in the four other pulsars (PSRs J0742+4110, J1045−0436, J1122−3546, and J2017−2737) that have "heuristic" energy fluxes, $G_h = \sqrt{\dot{E}}/4\pi d^2$, above the typical LAT detection threshold of 10^{15} (erg s^{-1})$^{1/2}$ kpc^{-2} (Abdo et al. 2013; Smith et al. 2019). This suggests that their DM-inferred distances could be underestimated, and/or that any beam of high-energy photons emitted by these pulsars do not intercept our line of sight. The latter is further supported by the large pulse width of these pulsars in the radio (all have duty cycles $\delta > 0.3$; see Table 1), which is generally indicative a low magnetic inclination and empirically associated with nondetection of gamma-ray pulsations (see, e.g., Rookyard et al. 2017; Smith et al. 2019; Johnston et al. 2020; Serylak et al. 2021).

[28] Data were downloaded from the LAT Data server available here: https://fermi.gsfc.nasa.gov/cgi-bin/ssc/LAT/LATDataQuery.cgi.
[29] Pass 8 data analysis (Bruel et al. 2018); see also the Fermi Science Support Center: https://fermi.gsfc.nasa.gov/ssc/data/analysis/documentation/Pass8_usage.html.
[30] https://github.com/nanograv/PINT

Table 4
Derived Common Properties of GBNCC Pulsars

PSR	P (s)	$\dot{P}$ (s s^{-1})	τ_c (yr)	B_{surf} (Gauss)	$\dot{E}$ (erg s^{-1})	D_{DM}^{NE2001} (kpc)	D_{DM}^{YMW16} (kpc)
J0405+3347	0.0639539495051(1)	$1.7(1) \times 10^{-19}$	6.1×10^{9}	3.3×10^{9}	2.5×10^{31}	1.9	1.7
J0742+4110	0.0031391369352908(3)	$6.692(5) \times 10^{-21}$	7.4×10^{9}	1.5×10^{8}	8.5×10^{33}	0.7	0.5
J1018−1523	0.0831525352278(3)	$1.09(6) \times 10^{-19}$	1.2×10^{10}	3.0×10^{9}	7.5×10^{30}	0.8	1.1
J1045−0436	0.024047517036698(1)	$7.8(1) \times 10^{-20}$	4.9×10^{9}	1.4×10^{9}	2.2×10^{32}	0.3	0.3
J1122−3546	0.007838069357439(3)	$1.53(7) \times 10^{-20}$	8.1×10^{9}	3.5×10^{8}	1.3×10^{33}	1.5	0.7
J1221−0633	0.0019345396958571(2)	$5.25(8) \times 10^{-21}$	5.8×10^{9}	1.0×10^{8}	2.9×10^{34}	0.8	1.2
J1317−0157	0.002908244599817(2)	$5.4(5) \times 10^{-21}$	8.6×10^{9}	1.3×10^{8}	8.6×10^{33}	2.8	25.0
J1742−0203	0.131609685521(9)	$1.5(1) \times 10^{-16}$	1.4×10^{7}	1.4×10^{11}	2.6×10^{33}	2.8	3.7
J2017−2737	0.22452428375(9)	$6.1(1) \times 10^{-15}$	5.8×10^{5}	1.2×10^{12}	2.1×10^{34}	1.0	1.6
J2018−0414	0.0406122096643(1)	$6(4) \times 10^{-20}$	1.1×10^{10}	1.5×10^{9}	3.3×10^{31}	1.5	1.8
J2022+2534	0.0026459357677905(3)	$6.16(1) \times 10^{-21}$	6.8×10^{9}	1.3×10^{8}	1.3×10^{34}	3.3	4.0
J2039−3616	0.0032750415513069(2)	$8.427(9) \times 10^{-21}$	6.2×10^{9}	1.7×10^{8}	9.5×10^{33}	0.9	1.7

Notes. D_{DM} is calculated using the NE2001 (Cordes & Lazio 2002) or YMW16 (Yao et al. 2017) Galactic free electron density models, as indicated. A fractional error of 50% is not uncommon. Derived parameters here have not been corrected for apparent acceleration caused by kinematic effects. $\dot{E}$ and B_{surf} are calculated assuming a moment of inertia $I = 10^{45}$ g cm^2; additionally, B_{surf} assumes a NS radius $R = 10$ km and $\alpha = 90°$ (angle between spin/magnetic axes). Calculating τ_c relies on the assumption that spin-down is fully due to magnetic dipole radiation (braking index, $n = 3$) and that the initial spin period is negligible. Values in parentheses are the 1σ uncertainty in the last digit, calculated by propagating uncertainties in measured parameters reported by TEMPO.

3.2.1. PSR J1221−0633

PSR J1221−0633 is spatially coincident with the bright Fermi source 4FGL J1221.4−0634. Here we consider the spin-down power of the pulsar to determine if the properties of the coincident 4FGL object are consistent with being the counterpart of PSR J1221−0633. The pulsar has a spin-down power of $\dot{E} = 2.9 \times 10^{34}$ erg s^{-1}, and assuming an average DM distance of 1 kpc, the corresponding heuristic flux $G_h \sim 10^{16}$ (erg s^{-1})$^{1/2}$ kpc^{-2} is well above the LAT threshold. The 4FGL-DR3 reports an integrated energy flux in the 0.1–100 GeV band, G_{100}, of 5.8×10^{-12} erg s^{-1} cm^{-2} for 4FGL J1221.4−0634. Assuming a gamma-ray beaming fraction $f_\Omega = 1$ (appropriate for outer-magnetosphere emission sweeping a full 4π steradians), the luminosity, L_γ, of the Fermi source ranges between 0.4 and 1×10^{33} erg s^{-1}, depending on the adopted DM distance. Comparing the power radiated in the 0.1–100 GeV band to the spin-down power, the gamma-ray conversion efficiency $\eta = L_\gamma/\dot{E}$ of 4FGL J1221.4−0634 is between 15 and 35%. These results are all consistent with 4FGL J1221.4−0634 being the counterpart of PSR J1221−0633.

Phase-folding the Fermi photons collected in the direction of PSR J1221−0633 resulted in strong pulsations ($H_{max} = 525$). The weight model that optimized the significance of the pulse profile had an energy scale $\mu_E = 3.7$ ($E_{ref} \approx 5$ GeV) and photons with $w > 1\%$. Figure 4 shows the binned gamma-ray pulse profile overlaid with the profiles of the pulsar at 350 and 820 MHz after barycentering the arrival times in both bands and correcting for time delays due to ISM propagation effects. The final timing ephemeris (Table 2) was used to calibrate the absolute phase alignment to the same reference time and frequency. In the radio band, PSR J1221−0633 displays two distinct peaks separated by ∼110° (or, equivalently, 0.31 in rotational phase), whereas only one broad component (pulse duty cycle δ of 0.18/0.35 at 50%/10% of the peak maximum intensity) is seen in the gamma-ray profile at the same rotational phase as the leading (and weaker) radio peak.[31] This is consistent with the gamma-ray and fainter radio beam being produced at a similar altitude (see, e.g., Johnson et al. 2014). These results further support the association of 4FGL J1221.4−0634 with PSR J1221−0633.

3.2.2. PSR J1317−0157

As previously mentioned, the point source 4FGL J1317.5−0153 is coincident with PSR J1317−0157 yet no gamma-ray pulsations were detected in the folded Fermi data. Despite having a spin-down luminosity ($\dot{E} \sim 9 \times 10^{33}$ erg s^{-1}) above the empirical gamma-ray emission deathline for MSPs ($\dot{E}_{death} = 8 \times 10^{32}$ erg s^{-1}; Guillemot et al. 2016), the large (and highly uncertain) distance predicted by the YMW16 model based on the DM along the pulsar line of sight ($D_{DM}^{YMW16} > 25$ kpc, i.e., exceeding the maximum Galactic contribution to the DM in that direction) translates into an energy flux G_h that is two orders of magnitude below the expected LAT sensitivity. To meet the LAT detectability threshold, the distance of the pulsar should be within ∼2.75 kpc, which is consistent with the distance predicted by the NE2001 model ($D_{DM}^{NE2001} = 2.8$ kpc). The Fermi point source has a 0.1–100 GeV flux of $G_{100} = 1.5 \times 10^{-12}$ erg s^{-1} cm^{-2}. Assuming a beaming fraction $f_\Omega = 1$, the gamma-ray luminosity of 4FGL J1317.5−0153 at the NE2001 distance is $L_\gamma = 1.4 \times 10^{33}$ erg s^{-1}. This translates into a gamma-ray efficiency $\eta = 16\%$, a typical value among known gamma-ray MSPs (see, e.g., Abdo et al. 2013; Smith et al. 2019). Apart from the overestimated/unconstrained YMW16 distance, the association of 4FGL J1317.5−0153 with PSR J1317−0157 is reasonable in terms of the expected Fermi-LAT sensitivity, the pulsar spin-down luminosity, and the low background level in that sky region. An unfavorable viewing geometry and/or magnetic alignment could explain the nondetection of gamma-

[31] We note that we used the zero-phase reference epoch in the timing solution as the fiducial phase. If instead we adopt the same approach as Abdo et al. (2013) and set the phase of the peak radio intensity as the fiducial phase, then the gamma-ray and weaker radio peaks of PSR J1221−0633 seen in Figure 4 are trailing the main radio peak by a phase of 0.69.

Table 5
Proper Motions and Kinematic Corrections for Three GBNCC Pulsars

PSR	μ_λ (mas yr^{-1})	μ_β (mas yr^{-1})	$D_{\rm DM}$ (kpc)	$v_{\rm t}$ (kms^{-1})	$\dot{P}_{\rm G}$ (10^{-21})	$\dot{P}_{\rm S}$ (10^{-21})	$\dot{P}_{\rm int}$ (10^{-21})	$B_{\rm surf}$ (10^8 G)	$\tau_{\rm c}$ (Gyr)	$\dot{E}$ (10^{33} erg s^{-1})
J0742+4110	−12(2)	−9(5)	0.7(2)	5(2) × 10^1	−0.01	1.27	5.43	1.3	9.2	6.9
			0.5(2)	4(1) × 10^1	−0.02	0.93	5.79	1.4	8.6	7.4
J2022+2534	−4.0(7)	−8(1)	3(1)	1.4(5) × 10^2	−0.83	1.77	5.22	1.2	8.0	11.1
			4(1)	1.7(6) × 10^2	−1.03	2.14	5.05	1.2	8.3	10.8
J2039−3616	−13.5(4)	2(1)	0.9(3)	6(2) × 10^1	−0.11	1.35	7.19	1.6	7.2	8.1
			1.7(5)	1.1(3) × 10^2	0.00	2.51	5.92	1.4	8.8	6.7

Notes. For each pulsar in this study with measurable proper motion, we list measurements in ecliptic longitude and latitude (μ_λ and μ_β). Distances estimated using pulsars' DMs and Galactic electron density models (top: NE2001; bottom: YMW16) are quoted with ≈30% uncertainty. Calculating transverse velocity (v_t) based on these quantities allows us to calculate, in turn, secular acceleration (the Shklovskii effect; $\dot{P}_{\rm S}$) and that due to pulsars' motion in the Galactic potential ($\dot{P}_{\rm G}$); removing these factors from $\dot{P}$ gives the intrinsic value, $\dot{P}_{\rm int}$, which is used to calculate derived quantities, surface magnetic field strength ($B_{\rm surf}$), characteristic age ($\tau_{\rm c}$), and spin-down luminosity ($\dot{E}$).

Table 6
DD Binary Parameters of PSR J1018−1523

Parameter	Value
Measured Parameters	
$P_{\rm B}$ (days)	8.9839727(6)
$a \sin i/c$ (s)	26.15662(3)
T_0 (MJD)	57545.74874(3)
e	0.227749(2)
ω (°)	60.013(1)
Derived Parameters	
f_M ($M_\odot$)	0.238062
$M_{\rm c,min}$ ($M_\odot$)	1.16
$\dot{\omega}$ (°yr^{-1})	0.010(1)
$m_{\rm tot}$ ($M_\odot$)	2.3(3)

Note. Values in parentheses are the 1σ uncertainty in the last digit as reported by TEMPO.

ray pulsations in this pulsar. Careful modeling of the radio profile evolution and polarization properties could help determine the validity of the magnetosphere-geometry argument for the nondetection at high energies (e.g., Rookyard et al. 2017). Such analysis is however beyond the scope of this work. It should also be noted that the 4FGL-DR3 catalog reports a 50% probability that this Fermi source is associated with the active galactic nucleus CRATES J1317−0159 (Healey et al. 2007). At this point, we cannot conclusively associate 4FGL J1317.5−0153 with PSR J1317−0157.

3.2.3. PSR J2039−3616

After correcting for the apparent accelerations that arise from kinematic effects (Section 2.4), the intrinsic spin-down power $\dot{E}$ and heuristic energy flux G_h we estimated for PSR J2039−3616 are $\dot{E} = 6.7 \times 10^{33}$ erg s^{-1} and $G_h = 2 \times 10^{15}$ (erg s^{-1})$^{1/2}$ kpc^{-2} when adopting the distance predicted by the YMW16 model ($D_{\rm DM}^{\rm YMW} = 1.7$ kpc), and $\dot{E} = 8.1 \times 10^{33}$ erg s^{-1} and $G_h = 9 \times 10^{15}$ (erg s^{-1})$^{1/2}$ kpc^{-2} for the NE2001 distance ($D_{\rm DM}^{\rm NE2001} = 0.9$ kpc). Both distance predictions are small enough to produce fluxes above the LAT sensitivity to point sources—in fact, LAT detectability ($G_h > 10^{15}$ (erg s^{-1})$^{1/2}$ kpc^{-2}) is ensured for a pulsar distance < 2.6 kpc.

The Fermi source coincident with J2039−3616, 4FGL J2039.4−3616, has a energy flux $G_{100} = 3.8 \times 10^{-12}$ erg s^{-1} cm^{-2}. When the distance predicted by NE2001 is adopted, the corresponding luminosity and efficiencies are $L_\gamma = 0.4 \times 10^{33}$ erg s^{-1} and $\eta = 5\%$. If instead the larger distance predicted by YMW16 is used, we obtain $L_\gamma = 1.3 \times 10^{33}$ erg s^{-1} and $\eta = 20\%$.

We also detected bright gamma-ray pulsed emission from PSR J2039−3616 when we phase-folded the Fermi photons. Filtering out photons with $w < 0.5\%$ and setting $\mu_E = 3.75$ yielded the strongest pulsations at a significance of $H_{\rm max} = 452$. The gamma-ray pulse profile of PSR J2039−3616 is relatively narrow (δ of 0.12/0.28 at 50%/10% of the peak intensity) and single peaked, and is aligned with the rotational phase of the main peak of the (complex) profile in both radio bands (see Figure 4). Phase alignment of the radio and gamma-ray beams suggests the colocation of emission regions across wave bands (Abdo et al. 2010b), possibly high in altitude and caustic in origin (Venter et al. 2012; Johnson et al. 2014). PSR J2039−3616 is an interesting target for testing emission geometry models: radio polarization information would be most helpful, however only total-intensity data were recorded on this pulsar for this project.

In light of the properties discussed above and the firm detection of pulsed GeV emission, we identify PSR J2039−3616 as the source powering 4FGL J2039.4−3616.

4. Discussion

4.1. Isolated Pulsars

Five pulsars (PSRs J0405+3347, J1122−3546, J1742−0203, J2017−2737, and J2018−0414) were included in this study based on their relatively high spin frequencies, possibly indicative of spin-up due to a previous recycling period. However, two show no signs of recycling (PSRs J1742−0203 and J2017−2737 appear to be young, canonical pulsars) and the other three do but are no longer bound to their binary companions.

4.1.1. Nonrecycled Pulsars

After its discovery, PSR J1742−0203 was considered a candidate binary pulsar due to its intermediate, 132 ms spin period. However, extended timing showed no evidence of the pulsar being in a binary system and, given its measured period derivative (1.5×10^{-16} s s^{-1}), it is also unlikely to be recycled. Although only a single attempt was made, PSR J1742−0203 was not detected at 820 MHz in a 5 min scan. Using the nondetection, we place an apparent upper limit on its flux density at 820 MHz, $S_{820} < 0.2$ mJy, using the

Table 7
ELL1 Binary Parameters of GBNCC Pulsars

PSR	Measured					Derived	
	P_B (days)	$a \sin i/c$ (s)	T_{asc} (MJD)	ϵ_1	ϵ_2	f_M ($M_\odot$)	$M_{c,min}$ ($M_\odot$)
J0742+4110	1.385361182(2)	0.556456(3)	56045.146865(2)	$1(1) \times 10^{-5}$	$-0(9) \times 10^{-6}$	9.6394×10^{-5}	0.06
J1045−0436	10.27364597(4)	22.252633(8)	57472.187456(2)	$-4.53(8) \times 10^{-5}$	$5.83(8) \times 10^{-5}$	1.1209×10^{-1}	0.82
J1221−0633	0.386349620(4)	0.0552855(7)	57906.123003(2)	$1.0(3) \times 10^{-4}$	$-1.0(2) \times 10^{-4}$	1.2155×10^{-6}	0.01
J1317−0157	0.089128297(2)	0.027795(4)	57909.041863(5)	$5(2) \times 10^{-4}$	$0(2) \times 10^{-4}$	2.9024×10^{-6}	0.02
J2022+2534	1.283702830(2)	0.6092405(6)	57535.5638685(8)	$2(2) \times 10^{-6}$	$3(2) \times 10^{-6}$	1.4734×10^{-4}	0.07
J2039−3616	5.789963674(4)	3.3975854(4)	57538.6033176(3)	$-5.1(3) \times 10^{-6}$	$-3.3(3) \times 10^{-6}$	1.2562×10^{-3}	0.14

Notes. All timing models presented here use the ELL1 binary model, which is appropriate for low-eccentricity orbits. Values in parentheses are the 1σ uncertainty in the last digit as reported by TEMPO.

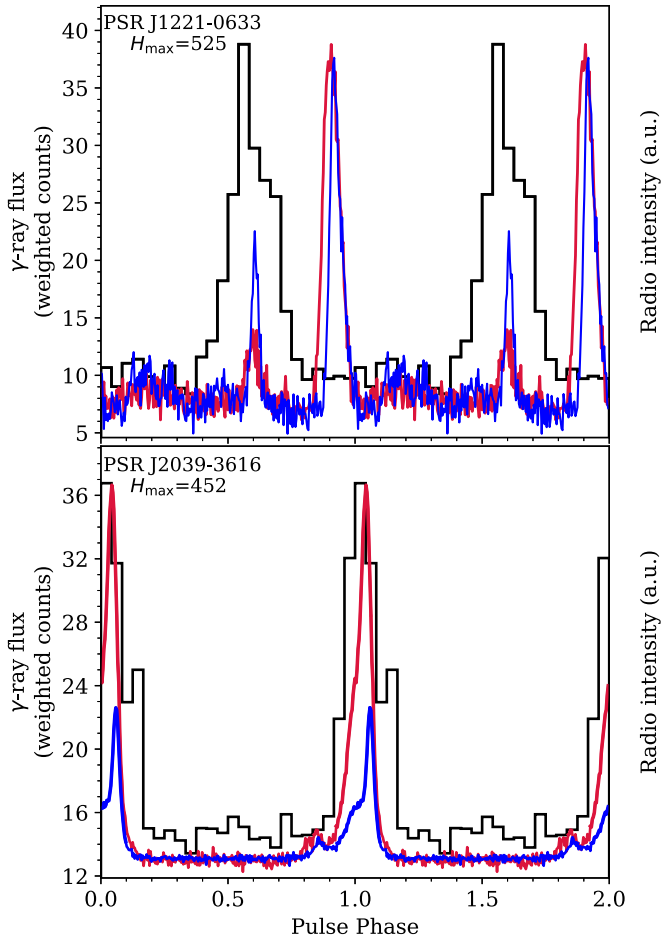

Figure 4. Gamma-ray (black) and radio pulse profiles at 350 MHz (red) and 820 MHz (blue) for PSRs J1221−0633 (top) and J2039−3616 (bottom), phase-aligned with their respective timing ephemerides (Section 3.1). The gamma-ray profiles were generated using the photon filtering and energy scaling that maximized the H-test value (see H_{max} in the top-left of each panel), as described in Section 3.2. All radio profiles are shown with 256 phase bins per cycle, while the gamma-ray profiles have 24 phase bins per cycle.

radiometer equation (assuming a duty cycle, $\delta = 0.06$ and S/N detection threshold of S/N > 6), which also constrains its spectral index, $\alpha < -1.5$. Since PSR J1742−0203 was never detected at 820 MHz, the DM value listed in Table 3 maximizes S/N in a high-S/N 350 MHz observation; we were not able to reliably fit for DM in TEMPO with single-frequency data, so we do not include a corresponding uncertainty in the table.

Similar to PSR J1742−0203, PSR J2017−2737 was considered as a candidate recycled pulsar due to its intermediate spin period, 225 ms. However, concerted timing efforts showed that its $\dot{P}$, and therefore derived B_{surf} values, were too large to indicate a previous period of recycling.

4.1.2. Disrupted Recycled Pulsars

PSR J0405+3347 is a solitary pulsar with a relatively short, 64 ms spin period and weak magnetic field ($B_{surf} = 3.3 \times 10^9$ G). Using the definition for a disrupted recycled pulsar (DRP) posed by Belczynski et al. (2010), an isolated pulsar in the Galactic disk, with $B < 3 \times 10^{10}$ G and $P > 20$ ms, PSR J0405+3347 is a new DRP. Its spin parameters indicate that it is partially recycled, but the recycling process was likely cut short when its companion went supernova, disrupting the system and producing an isolated, young pulsar and a partially recycled isolated pulsar (e.g., see discussion of J1821+0155 in Rosen et al. 2013). Although its period derivative is not as well constrained, PSR J2018−0414 too has a short, 41 ms spin period and likely evolved via the same mechanism as PSR J0405+3347.

4.1.3. PSR J1122−3546

PSR J1122−3546 is an isolated MSP with a 7.8 ms spin period. It is widely accepted that MSPs have such short spin periods as a result of an extended recycling process, where material from a binary companion transfers angular momentum, "spinning up" the pulsar (Alpar et al. 1982). Consistent with this evolutionary theory, we find the majority of MSPs reside in near-circular orbit binary systems with low-mass white dwarf (WD) companions.[32] Isolated MSPs like PSR J1122−3546 are comparatively uncommon, comprising roughly 25% of the MSP population in the Galactic field, but their evolutionary history remains an open question.

4.2. Millisecond Pulsars Suitable for Pulsar Timing Arrays

The primary science goal for the GBNCC pulsar survey is discovering new MSPs, particularly those suitable for high-precision timing in the effort to use PTAs to detect low-frequency GWs. Generally, bright MSPs with short spin periods and sharp features in their profile are best, ideally producing TOAs with timing residuals that have rms <1 μs (at observing frequencies $\gtrsim 1$ GHz). Both PSRs J2022+2534 and J2039−3616 satisfy these basic criteria, and therefore have

[32] See, e.g., http://www.atnf.csiro.au/research/pulsar/psrcat (Manchester et al. 2005).

been added to the NANOGrav PTA for use in low-frequency GW detection and characterization.

PSR J2022+2534 is a 2.6 ms pulsar in a short, 1.3 day circular orbit around a low-mass ($m_{c,min} = 0.07\ M_\odot$) companion. Its eccentricity is close to zero, which is typical for MSPs, whose long recycling periods tend to circularize their orbits (Phinney & Kulkarni 1994). Although this pulsar appears to be bright across the frequency spectrum between 300 MHz and 2.5 GHz,[33] its profile is broad (duty cycle $\delta > 0.5$) and lacks narrow features at 350 MHz, which makes timing imprecise at low observing frequencies. Figure 3 shows a comparison between TOA precision at 350 MHz versus 820 MHz. At 820 MHz and higher observing frequencies, PSR J2022+2534 remains bright, and although its average profile envelope is still broad sharp features provide consistent anchors for profile template matching, making it a promising candidate for PTA science.

PSR J2022+2534 has been added to the NANOGrav PTA—initially monitored at the Arecibo Observatory, but now regularly at the Green Bank Observatory and with the Canadian Hydrogen Intensity Mapping Experiment (CHIME; CHIME/Pulsar Collaboration et al. 2021) telescope—and it will continued to be monitored closely in the coming years to ensure long-term timing stability necessary for MSPs used to detect GWs.

PSR J2039−3616 is a 3.3 ms pulsar in a 5.8 day, nearly circular orbit about a (likely) low-mass WD companion. Like PSR J2022+2534, PSR J2039−3616 remains bright up to observing frequencies of 2.5 GHz[34] and its sharp profile makes it a good PTA candidate; observing at 820 MHz and above, individual TOA uncertainties are typically <1 μs, so PSR J2039−3616 has been included in NANOGrav's PTA. PSR J2039−3616 is near Green Bank Observatory's low declination limit (GBO can observe sources with decl. $\gtrsim -45°$), so this pulsar may also prove useful for PTA experiments with better access to Southern Hemisphere sources, like the Parkes Pulsar Timing Array (Reardon et al. 2021), the Indian Pulsar Timing Array (Joshi et al. 2018), and MeerTime (Miles et al. 2022).

For PSR J2039−3616, in addition to proper motion (see Table 3), we find a significant measurement of parallax, 5.5 ± 1.2 mas, implying a distance of 182^{+51}_{-33} pc, which is about 10 times closer than the DM distance estimates. Estimating pulsar distances using DM can be unreliable for sources away from the plane, and PSR J2039−3616 has a Galactic latitude $b = -36.^\circ5$. However, since the data included in this study span only 2 yr, we have have not included parallax in our final timing model fits and we hope to revisit this discrepancy with a longer timing baseline; the changes to other parameters when parallax is included are within their uncertainties published here. There are no Gaia counterparts within 5′ of PSR J2039−3616 (Gaia Collaboration et al. 2016, 2022).

4.3. Black Widow Systems

Both PSRs J1221−0633 and J1317−0157 are in tight (<10 hr) orbits, they likely have very low-mass companions ($M_c < 0.05\ M_\odot$), and both exhibit eclipses (see Figure 5); all of these traits are consistent with "black widow" systems (Fruchter et al. 1988; Roberts 2011) in which pulsars are actively ablating their companions. As a result, a large amount of intrabinary material is present, which can cause the pulsar signal to be additionally dispersed or completely obscured around superior conjunction. Sections 3.2.1 and 3.2.2 describe our findings that PSRs J1221−0633 and J1317−0157 have Fermi-LAT gamma-ray counterparts, with the former also exhibiting gamma-ray pulsations.

PSR J1221−0633 was confirmed at 350 MHz as a new, nearby MSP, with a 1.9 ms spin period and estimated DM distance of ≈1 kpc. It has a relatively broad, single-component profile and faint signal at 350 MHz, but exhibits much higher S/N and a complex, multicomponent profile at 820 MHz (see Figure 1). Once a preliminary set of orbital parameters revealed PSR J1221−0633's short orbital period ($P_B = 9.26$ hr), a long, 2.5 hr scan was scheduled spanning superior conjunction to check for signs of eclipsing. Figure 5 shows the additional ≈200 μs delay in pulse arrival times at 820 MHz around superior conjunction, likely due to dispersion as the pulsar signal travels through plasma surrounding the companion (not Shapiro delay). This delay suggests an extra electron column density of $\approx 10^{17}$ cm^{-2}, which is comparable to similar measurements for other systems (Stappers et al. 2001; Freire 2005). Although the duration of eclipses for pulsars in black widow systems is known to vary from one orbit to the next, our scan from MJD 58098 shows both ingress at $\phi_{orb} \approx 0.17$ and egress at $\phi_{orb} \approx 0.33$, so the pulsar signal is affected over ≈16% of an orbit (about 1.5 hr).

PSR J1317−0157 is a 2.9 ms pulsar in a 2.14 hr orbit and, like PSR J1221−0633, it is also a new black widow system that shows signs of eclipses around superior conjunction. Unlike PSR J1221−0633, we have not detected this pulsar's signal *during* eclipses, but, on MJD 58116, PSR J1317−0157 was observed coming out of an eclipse during a 20 minute scan. In this observation, the pulsar's signal was obscured for ≈500 s, placing a lower limit on the duration of eclipse (≈6.5% of the orbit). The lack of detections over 10%−15% of the orbit (see Figure 5) suggests eclipses in this case tend to last for 13−20 mins.

With estimates for the duration of eclipses for both PSRs J1221−0633 and J1317−0157, and assuming inclination angles of 90°, we place limits on each companion's radius, $R_{c,min\ J1221} = 1.2\ R_\odot$ and $R_{c,min\ J1317} = 0.43\ R_\odot$. Also assuming edge-on orbits and pulsar masses $m_p = 1.4\ M_\odot$, the orbital separations are $a_{J1221} = 2.5\ R_\odot$ and $a_{J1317} = 0.94\ R_\odot$, and (based on Eggleton 1983), the Roche-lobe radius for each system is much smaller than the corresponding radius of each eclipsing object (by a factor of 5 in both cases). PSRs J1221−0633 and J1317−0157 have companions with unbound plasma clouds, indicating that they are losing mass.

4.4. PSR J0742+4110

PSR J0742+4110 is a 3.1 ms pulsar in a short, 1.4 day orbit around a low-mass ($m_{c,min} = 0.06\ M_\odot$) companion. Originally found in 2012, it was first published among the first batch of 67 GBNCC discoveries (Stovall et al. 2014), but initial timing follow-up was conducted using an incorrect position. As a result, deriving a coherent timing solution for this pulsar was significantly delayed. PSR J0742+4110 has a DM distance <1 kpc (see Table 5), it appears to be relatively bright, and has a shallow spectrum (see Table 1); however, its profile is broad

[33] Higher-frequency testing done at the Arecibo Observatory by Andrew Seymour, private communication.
[34] Higher-frequency testing done at Green Bank Observatory by the NANOGrav Collaboration, private communication.

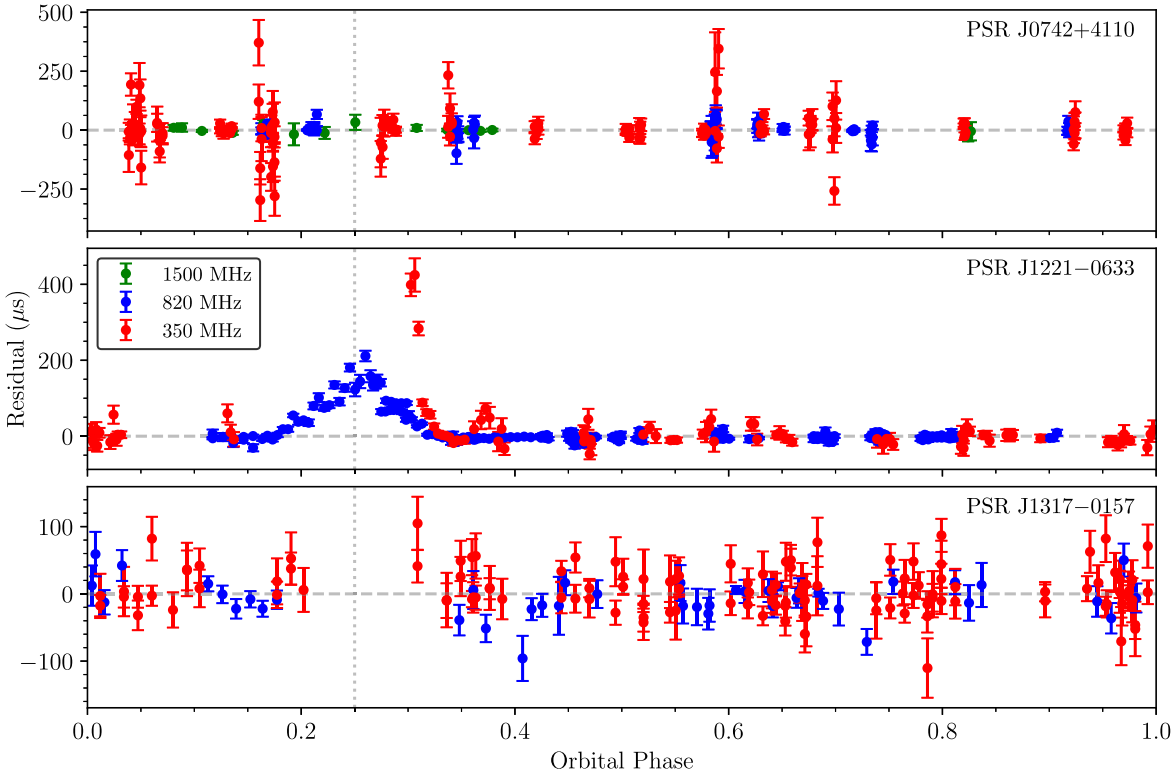

Figure 5. Residuals from PSRs J0742+4110, J1221−0633, and J1317−0157 plotted against orbital phase. Superior conjunction at $\phi_{\rm orb} = 0.25$ is shown with a dotted line. The lack of detections at or near superior conjunction indicates that the signal from PSR J1317−0157 is likely being eclipsed by its WD companion, and dispersive delays in PSR J1221−0633's signal while behind its companion indicate partial eclipsing. Based on PSR J0742+4110's residuals, there appears to be no sign of eclipse.

and lacks sharp features that might otherwise make it suitable for use in PTAs. Despite this, we measure significant proper motion for this pulsar (see Table 3), likely because of the comparatively longer timing baseline than other MSPs included here. The low companion mass for PSR J0742+4110 is near the threshold for those typical of black widow systems; however, in combination with its orbital period, PSR J0742+4110's properties are inconsistent with those of the black widow population. We also do not see any evidence of eclipsing or excess dispersion delays around superior conjunction (see Figure 5).

4.5. PSR J1018−1523

PSR J1018−1523 is a recycled, 83 ms pulsar in an eccentric ($e = 0.23$), 9 day orbit around a massive companion. Assuming a typical pulsar mass of 1.4 $M_\odot$, the minimum companion mass is $m_{\rm c,min} = 1.16\ M_\odot$. Based on the large companion mass and orbital eccentricity, PSR J1018−1523 is likely a new DNS system (for other examples, see Tauris et al. 2017). In addition to the five Keplerian parameters describing its orbit, we also find a significant change in the angle of periastron over time ($\dot{\omega}$; see Table 6), which is a relativistic effect predicted by general relativity. Compared to other known DNS systems (a summary of which is provided in Tauris et al. 2017), the Keplerian parameters here fall within typical ranges. The total mass derived from the advance of periastron ($\dot{\omega}$), $m_{\rm tot} = 2.3 \pm 0.3$ $M_\odot$, is comparatively low, but it is consistent with other DNS systems to within 1σ uncertainty (Abbott et al. 2017; Tauris et al. 2017; Abbott et al. 2020). Although PSR J1018−1523 is not expected to merge within a Hubble time, future work to improve the precision of its advance of periastron and possibly measure one or more additional post-Keplerian parameters will aid in constraining Galactic NS mass distributions (see, e.g., Farrow et al. 2019).

4.6. PSR J1045−0436

Although initially discovered as a bright candidate, five follow-up scans were needed to confirm PSR J1045−0436, and in future timing efforts the pulsar was unreliably detected at both 350 and 820 MHz. PSR J1045−0436 has a 24 ms spin period and orbits an intermediate-mass ($m_{\rm c,min} = 0.82\ M_\odot$) WD companion every 10.3 days. With a nearly circular orbit, PSR J1045−0436's characteristics are similar to those of other intermediate-mass binary pulsars (IMBPs; e.g., Camilo et al. 2001; Lorimer 2008), and most likely has a CO WD companion. There has been no correlation found between orbital phase and detectability, but because of its low DM (4.8 pc cm^{-3}), significant variability in the pulsar's apparent flux density due to scintillation is plausible. Yao et al. (2017) estimates PSR J1045−0436 has a scintillation timescale ($\Delta t = 2000$ s) longer than a typical scan length and scintillation bandwidth ($\Delta f = 130$ MHz) comparable to the observing bandwidth at 820 MHz. Assuming the DM distance is correct, PSR J1045−0436 has a height above the Galactic plane of $|z| \approx 0.2$ kpc, which is consistent with other IMBPs (Camilo et al. 2001).

4.7. Optical Constraints

For all of the binary pulsar systems in this study with nearly circular orbits (see Table 7), we have checked the source catalogs of the Pan-STARRS 3π Steradian Survey (Chambers

et al. 2016) for sources north of $\delta = -30°$ and SkyMapper (Onken et al. 2019) for other sources and find no optical/IR counterparts coincident with positions measured via pulsar timing.

Using the same procedure as that outlined in earlier studies (Kawash et al. 2018; Lynch et al. 2018), we use the average 5σ magnitude lower limits for the PS1 *griz* bands (23.3, 23.2, 23.1, and 22.3, respectively; Chambers et al. 2016) to place constraints on PSR J1045−0436's CO-core WD companion (assuming an orbital inclination angle of 60° to calculate a median companion mass $M_{\rm c,med} = 1.0\ M_\odot$). We also estimate reddening along the line of sight based on a 3D map of interstellar dust reddening (Green et al. 2019) and the largest (most conservative) DM distance estimate available (see Table 4). Reddening values are converted to extinctions in PS1 bands using Table 6 in Schlafly & Finkbeiner (2011). Comparing dereddened magnitude limits to corresponding hydrogen-atmosphere cooling models[35] from Bergeron et al. (2011), we find the *i*-band limit to be the most constraining, limiting PSR J1045−0436's companion to an effective temperature $T_{\rm eff} < 5200$ K and age >8.3 Gyr for the median companion mass.

PSR J2039−3616 likely has a He-core WD companion based on its companion mass, $M_{\rm c,med} = 0.17\ M_\odot$ (see Table 7). Since this source is outside the region of sky coverered by Pan-STARRS, we use average 5σ *griz* limits from SkyMapper instead (22, 22, 21, and 20, respecively; Onken et al. 2019). We use extremely low-mass (ELM) evolutionary models from Althaus et al. (2013) together with hydrogen model atmospheres from Bergeron et al. (2011) to find that the *r*-band limit constrains the effective temperature to be $T_{\rm eff} < 7800$ K for an assumed radius of $0.04\ R_\odot$. We verified that this radius is consistent with expectations for a $0.17\ M_\odot$ ELM WD based on custom-made evolutionary models computed following Istrate et al. (2016). Note that in this regime ELM WDs do not exhibit hydrogen shell flashes but cool steadily, allowing us to limit the age to >9.8 Gyr since the end of Roche-lobe overflow. However, at lower inclinations, <45°, or with a more massive pulsar the companion mass could exceed $0.2\ M_\odot$ and then the age constraint would not be useful.

Through pulsar timing, we find median masses for the remaining companions to be $\ll 0.1\ M_\odot$, which is below the range of expected WD masses (see, e.g., Istrate et al. 2016). Instead these are likely "black widow" or "redback" companions that are the remains of partially degenerate stars ablated by the pulsars. To constrain any possible companion, we first calculate Roche-lobe radii for the companions based on Eggleton (1983). We then assume that the companions have a volumetric Roche-lobe filling factor of 50%. Using the main-sequence colors from Covey et al. (2007) together with the main-sequence radii from Pecaut & Mamajek (2013), we infer effective temperature limits of <2800 K for J0742+4110, J1221−0633, and J2022+2534 (note that the limits for these sources could be more constraining, but this is the coolest effective temperature in the model grids). For J1317−0157 we have a less constraining limit of $T_{\rm eff} < 4800$ K. Even for Roche-lobe filling fractions of 10% the limits on J0742+4110, J1221−0633, and J2022+2534 stay at <2800 K, which are consistent with typical nightside temperatures for known black widow systems (e.g., Breton et al. 2013; Dhillon et al. 2022).

We also examined archival data available through the Aladin server[36] for associated diffuse structures such as pulsar wind nebulae (PWN) and supernova remnants (SNRs). Across all available wavelengths for each of the 12 pulsars, we searched for both cataloged objects and for symmetric diffuse emission reminiscent of a previously unidentified SNR or PWN. No plausible structures were found.

4.8. Gamma-Ray Pulsars

Two of our pulsars—PSRs J1221–0633 and J2039–3616—show detectable, pulsed gamma-ray emission (see Sections 3.2.1 and 3.2.3). The gamma-ray efficiencies of 5%–35% are similar to those measured for other MSPs from which gamma rays have been detected (Acero et al. 2015). As shown in Figure 4, the radio profile of PSR J1221–0633 has two components, with the gamma-ray peak aligning with the weaker component. Conversely, the radio profile of PSR J2039–3616 has only one component, and it is aligned with the gamma-ray profile. These properties appear to be broadly representative of those of MSPs published in the Fermi Second Pulsar Catalog, in which 27 MSPs had misaligned radio/gamma-ray profiles and six had aligned radio/gamma-ray profiles (Acero et al. 2015). Misaligned profiles are easily interpreted with standard "slot gap" or "outer gap" emission models with narrow beams, while the aligned profiles require both the radio and gamma-ray emission to originate in the outer-gap region. Aligned MSPs may be more likely to have low linear polarization due to caustic emission over a wide range of altitudes. Future polarization studies could test this hypothesis for PSR J2039–3616. In addition, Acero et al. (2015) found that pulsars with aligned radio/gamma-ray profiles generally had higher values of magnetic field at the light cylinder. PSR J2039–3616 does not seem to fit this picture, however, as its magnetic field at the light cylinder is 4.4×10^4 G and the mean value for the MSP population (i.e., periods greater than 30 ms) is 8.5×10^4 G.

5. Conclusion

We present coherent timing solutions for 12 pulsars discovered by the GBNCC pulsar survey. Seven of these discoveries are in binary systems: five MSPs orbiting low-mass WD companions (including two black widow systems that eclipse and two high-precision timers suitable for PTAs), one IMBP, and a new DNS system. Our results show that three discoveries (an isolated MSP and two DRPs) evolved via interaction with binary companions sometime in the past and two more are younger, isolated, and nonrecycled pulsars. These results underscore the importance of long-term pulsar timing; classifying evolutionary histories of systems like these requires spin-down measurements, which can only be obtained with data spanning 1 yr or more.

Since 2020, the GBNCC collaboration has been partnering with the CHIME Pulsar collaboration to extend existing pulsar timing solutions and rapidly follow up on new discoveries at decl. $\delta \gtrsim -15°$. We are now regularly timing over 130 pulsars with CHIME, including several from this study, and those results will be presented in future work.

[35] http://www.astro.umontreal.ca/~bergeron/CoolingModels/

[36] https://aladin.u-strasbg.fr/

The Green Bank Observatory is a facility of the National Science Foundation (NSF) operated under cooperative agreement by Associated Universities, Inc. The National Radio Astronomy Observatory is a facility of the NSF operated under cooperative agreement by Associated Universities, Inc. J.K.S., D.L.K., M.A.M., M.E.D., T.D., S.M.R., and X.S. are supported by the NANOGrav NSF Physics Frontiers Center award numbers 1430284 and 2020265. E.P. is supported by an H2020 ERC Consolidator Grant "MAGNESIA" under grant agreement No. 817661 and National Spanish grant No. PGC2018-095512-BI00. Z.P. is a Dunlap Fellow. J.vL. acknowledges funding from the European Research Council under the European Unions Seventh Framework Programme (FP/2007-2013) / ERC Grant Agreement n. 617199 ("ALERT"), and from Vici research program "ARGO" with project number 639.043.815, financed by the Netherlands Organisation for Scientific Research (NWO). M.A.M. and E.F. L. are supported by NSF OIA-1458952 and NSF Award Number 2009425. S.M.R. is a CIFAR Fellow. Pulsar research at UBC is supported by an NSERC Discovery Grant and by the Canadian Institute for Advanced Research. M.S. acknowledges funding from the European Research Council (ERC) under the European Unions Horizon 2020 research and innovation program (grant agreement No. 694745). M.E.D. acknowledges support from the Naval Research Laboratory by NASA under contract S-15633Y. This work has made use of data from the European Space Agency (ESA) mission Gaia (https://www.cosmos.esa.int/gaia), processed by the Gaia Data Processing and Analysis Consortium (DPAC; https://www.cosmos.esa.int/web/gaia/dpac/consortium). Funding for the DPAC has been provided by national institutions, in particular the institutions participating in the Gaia Multilateral Agreement. T.D. is supported by an NSF Astronomy and Astrophysics Grant (AAG) award number 2009468.

Facility: GBT (GUPPI).

Software: `PRESTO` (https://www.cv.nrao.edu/~sransom/presto/), `PSRCHIVE` (Hotan et al. 2004), `TEMPO` (http://tempo.sourceforge.net/), `PyGDSM` (https://github.com/telegraphic/pygdsm), `PINT` (https://github.com/nanograv/PINT), `PyGEDM` (https://github.com/FRBs/pygedm).

ORCID iDs

J. K. Swiggum https://orcid.org/0000-0002-1075-3837
Z. Pleunis https://orcid.org/0000-0002-4795-697X
E. Parent https://orcid.org/0000-0002-0430-6504
D. L. Kaplan https://orcid.org/0000-0001-6295-2881
M. A. McLaughlin https://orcid.org/0000-0001-7697-7422
I. H. Stairs https://orcid.org/0000-0001-9784-8670
R. Spiewak https://orcid.org/0000-0002-6730-3298
G. Y. Agazie https://orcid.org/0000-0001-5134-3925
P. Chawla https://orcid.org/0000-0002-3426-7606
M. E. DeCesar https://orcid.org/0000-0002-2185-1790
T. Dolch https://orcid.org/0000-0001-8885-6388
W. Fiore https://orcid.org/0000-0001-5645-5336
E. Fonseca https://orcid.org/0000-0001-8384-5049
A. G. Istrate https://orcid.org/0000-0002-8811-8171
V. M. Kaspi https://orcid.org/0000-0001-9345-0307
V. I. Kondratiev https://orcid.org/0000-0001-8864-7471
J. van Leeuwen https://orcid.org/0000-0001-8503-6958
L. Levin https://orcid.org/0000-0002-2034-2986
E. F. Lewis https://orcid.org/0000-0002-2972-522X
R. S. Lynch https://orcid.org/0000-0001-5229-7430
A. E. McEwen https://orcid.org/0000-0001-5481-7559
H. Al Noori https://orcid.org/0000-0002-4187-4981
S. M. Ransom https://orcid.org/0000-0001-5799-9714
X. Siemens https://orcid.org/0000-0002-7778-2990
M. Surnis https://orcid.org/0000-0002-9507-6985

References

Abbott, B. P., Abbott, R., Abbott, T. D., et al. 2017, PhRvL, 119, 161101
Abbott, B. P., Abbott, R., Abbott, T. D., et al. 2020, ApJL, 892, L3
Abdo, A. A., Ackermann, M., Ajello, M., et al. 2010a, ApJS, 187, 460
Abdo, A. A., Ackermann, M., Ajello, M., et al. 2010b, ApJ, 712, 957
Abdo, A. A., Ajello, M., Allafort, A., et al. 2013, ApJS, 208, 17
Abdollahi, S., Acero, F., Baldini, L., et al. 2022, ApJS, 260, 53
Acero, F., Ackermann, M., Ajello, M., et al. 2015, ApJS, 218, 23
Agazie, G. Y., Mingyar, M. G., McLaughlin, M. A., et al. 2021, ApJ, 922, 35
Alam, M. F., Arzoumanian, Z., Baker, P. T., et al. 2021a, ApJS, 252, 4
Alam, M. F., Arzoumanian, Z., Baker, P. T., et al. 2021b, ApJS, 252, 5
Aloisi, R. J., Cruz, A., Daniels, L., et al. 2019, ApJ, 875, 19
Alpar, M. A., Cheng, A. F., Ruderman, M. A., & Shaham, J. 1982, Natur, 300, 728
Althaus, L. G., Miller Bertolami, M. M., & Córsico, A. H. 2013, A&A, 557, A19
Antoniadis, J., Arzoumanian, Z., Babak, S., et al. 2022, MNRAS, 510, 4873
Arzoumanian, Z., Baker, P. T., Blumer, H., et al. 2020, ApJL, 905, L34
Atwood, W. B., Abdo, A. A., Ackermann, M., et al. 2009, ApJ, 697, 1071
Belczynski, K., Lorimer, D. R., Ridley, J. P., & Curran, S. J. 2010, MNRAS, 407, 1245
Bergeron, P., Wesemael, F., Dufour, P., et al. 2011, ApJ, 737, 28
Bhattacharyya, B., & Nityananda, R. 2008, MNRAS, 387, 273
Breton, R. P., van Kerkwijk, M. H., Roberts, M. S. E., et al. 2013, ApJ, 769, 108
Bruel, P. 2019, A&A, 622, A108
Bruel, P., Burnett, T. H., Digel, S. W., et al. 2018, arXiv:1810.11394
Burgay, M., D'Amico, N., Possenti, A., et al. 2003, Natur, 426, 531
Camilo, F., Lyne, A. G., Manchester, R. N., et al. 2001, ApJL, 548, L187
Camilo, F., Kerr, M., Ray, P. S., et al. 2015, ApJ, 810, 85
Capitaine, N., Wallace, P. T., & Chapront, J. 2003, A&A, 412, 567
Chambers, K. C., Magnier, E. A., Metcalfe, N., et al. 2016, arXiv:1612.05560
CHIME/Pulsar Collaboration, Amiri, M., Bandura, K. M., et al. 2021, ApJS, 255, 5
Chruslinska, M., Belczynski, K., Klencki, J., & Benacquista, M. 2018, MNRAS, 474, 2937
Cordes, J. M., & Lazio, T. J. W. 2002, ArXiv Astrophysics, arXiv:astro-ph/0207156
Covey, K. R., Ivezić, Ž, Schlegel, D., et al. 2007, AJ, 134, 2398
Cromartie, H. T., Camilo, F., Kerr, M., et al. 2016, ApJ, 819, 34
Cromartie, H. T., Fonseca, E., Ransom, S. M., et al. 2020, NatAs, 4, 72
Damour, T., & Deruelle, N. 1986, AnHP, 44, 263
de Jager, O. C., & Busching, I. 2010, A&A, 517, L9
Deneva, J. S., Ray, P. S., Camilo, F., et al. 2021, ApJ, 909, 6
Dhillon, V. S., Kennedy, M. R., Breton, R. P., et al. 2022, MNRAS, 516, 2792
Eggleton, P. P. 1983, ApJ, 268, 368
Farrow, N., Zhu, X.-J., & Thrane, E. 2019, ApJ, 876, 18
Freire, P. C. C. 2005, in ASP Conf. Ser. 328, Binary Radio Pulsars, ed. F. A. Rasio & I. H. Stairs (San Francisco, CA: ASP), 405
Fruchter, A. S., Stinebring, D. R., & Taylor, J. H. 1988, Natur, 333, 237
Gaia Collaboration, Prusti, T., de Bruijne, J. H. J., et al. 2016, A&A, 595, A1
Vallenari, A., Brown, A. G. A., Gaia Collaboration, et al. 2022, arXiv:2208.00211
GRAVITY Collaboration, Abuter, R., Amorim, A., et al. 2021, A&A, 647, A59
Green, G. M., Schlafly, E., Zucker, C., Speagle, J. S., & Finkbeiner, D. 2019, ApJ, 887, 93
Grishchuk, L. P. 2005, PhyU, 48, 1235
Guillemot, L., Smith, D. A., Laffon, H., et al. 2016, A&A, 587, A109
Guo, Y. J., Freire, P. C. C., Guillemot, L., et al. 2021, A&A, 654, A16
Hale, C. L., McConnell, D., Thomson, A. J. M., et al. 2021, PASA, 38, e058
Healey, S. E., Romani, R. W., Taylor, G. B., et al. 2007, ApJS, 171, 61
Holmberg, J., & Flynn, C. 2004, MNRAS, 352, 440
Hotan, A. W., van Straten, W., & Manchester, R. N. 2004, PASA, 21, 302
Istrate, A. G., Marchant, P., Tauris, T. M., et al. 2016, A&A, 595, A35
Jaffe, A. H., & Backer, D. C. 2003, ApJ, 583, 616
Johnson, T. J., Venter, C., Harding, A. K., et al. 2014, ApJS, 213, 6

Johnston, S., Smith, D. A., Karastergiou, A., & Kramer, M. 2020, MNRAS, 497, 1957
Jones, M. L., McLaughlin, M. A., Lam, M. T., et al. 2017, ApJ, 841, 125
Joshi, B. C., Arumugasamy, P., Bagchi, M., et al. 2018, JApA, 39, 51
Kalogera, V., Kim, C., Lorimer, D. R., et al. 2004, ApJL, 601, L179
Kaplan, D. L., Stovall, K., Ransom, S. M., et al. 2012, ApJ, 753, 174
Karako-Argaman, C., Kaspi, V. M., Lynch, R. S., et al. 2015, ApJ, 809, 67
Kawash, A. M., McLaughlin, M. A., Kaplan, D. L., et al. 2018, ApJ, 857, 131
Kerr, M., Camilo, F., Johnson, T. J., et al. 2012, ApJL, 748, L2
Lange, C., Camilo, F., Wex, N., et al. 2001, MNRAS, 326, 274
Lorimer, D. R. 2008, LRR, 11, 8
Lorimer, D. R., & Kramer, M. 2004, Handbook of Pulsar Astronomy (Cambridge: Cambridge Univ. Press)
Lynch, R. S., Swiggum, J. K., Kondratiev, V. I., et al. 2018, ApJ, 859, 93
Maggiore, M. 2000, PhR, 331, 283
Manchester, R. N., Hobbs, G. B., Teoh, A., & Hobbs, M. 2005, AJ, 129, 1993
Mandel, I., & Broekgaarden, F. S. 2022, LRR, 25, 1
McEwen, A. E., Spiewak, R., Swiggum, J. K., et al. 2020, ApJ, 892, 76
Miles, M. T., Shannon, R. M., Bailes, M., et al. 2022, MNRAS, 519, 3976
Onken, C. A., Wolf, C., Bessell, M. S., et al. 2019, PASA, 36, e033
Parent, E., Chawla, P., Kaspi, V. M., et al. 2020, ApJ, 904, 92
Pecaut, M. J., & Mamajek, E. E. 2013, ApJS, 208, 9
Perera, B. B. P., DeCesar, M. E., Demorest, P. B., et al. 2019, MNRAS, 490, 4666
Phinney, E. S., & Kulkarni, S. R. 1994, ARA&A, 32, 591
Pleunis, Z., Bassa, C. G., Hessels, J. W. T., et al. 2017, ApJL, 846, L19
Ransom, S. M., Eikenberry, S. S., & Middleditch, J. 2002, AJ, 124, 1788
Ransom, S. M., Ray, P. S., Camilo, F., et al. 2011, ApJL, 727, L16
Ray, P. S., Abdo, A. A., Parent, D., et al. 2012, arXiv:1205.3089
Reardon, D. J., Shannon, R. M., Cameron, A. D., et al. 2021, MNRAS, 507, 2137
Reid, M. J., & Brunthaler, A. 2020, ApJ, 892, 39
Roberts, M. S. E. 2011, in AIP Conf. Ser. 1357, Radio Pulsars: An Astrophysical Key to Unlock the Secrets of the Universe, ed. M. Burgay et al. (Melville, NY: AIP), 127
Rookyard, S. C., Weltevrede, P., Johnston, S., & Kerr, M. 2017, MNRAS, 464, 2018
Rosen, R., Swiggum, J., McLaughlin, M. A., et al. 2013, ApJ, 768, 85
Schlafly, E. F., & Finkbeiner, D. P. 2011, ApJ, 737, 103
Serylak, M., Johnston, S., Kramer, M., et al. 2021, MNRAS, 505, 4483
Shklovskii, I. S. 1970, SvA, 13, 562
Siemens, X., Ellis, J., Jenet, F., & Romano, J. D. 2013, CQGra, 30, 224015
Smith, D. A., Bruel, P., Cognard, I., et al. 2019, ApJ, 871, 78
Spiewak, R., Bailes, M., Miles, M. T., et al. 2022, PASA, 39, e027
Stappers, B. W., Bailes, M., Lyne, A. G., et al. 2001, MNRAS, 321, 576
Stovall, K., Lynch, R. S., Ransom, S. M., et al. 2014, ApJ, 791, 67
Swiggum, J. K., & Gentile, P. A. 2018, arXiv:1808.06643
Swiggum, J. K., Kaplan, D. L., McLaughlin, M. A., et al. 2017, ApJ, 847, 25
Tauris, T. M., Kramer, M., Freire, P. C. C., et al. 2017, ApJ, 846, 170
Taylor, J. H. 1992, RSPTA, 341, 117
Venter, C., Johnson, T. J., & Harding, A. K. 2012, ApJ, 744, 34
Vigna-Gomez, A., Neijssel, C. J., Stevenson, S., et al. 2018, MNRAS, 481, 4009
Will, C. M. 2014, LRR, 17, 4
Yao, J. M., Manchester, R. N., & Wang, N. 2017, ApJ, 835, 29
Zheng, H., Tegmark, M., Dillon, J. S., et al. 2017, MNRAS, 464, 3486